Journal of Power Sources 195 (2010) 638–648

Contents lists available at ScienceDirect

Journal of Power Sources

journal homepage: www.elsevier.com/locate/jpowsour

A new Pt–Rh carbon nitride electrocatalyst for the oxygen reduction reaction in polymer electrolyte membrane fuel cells: Synthesis, characterization and single-cell performance

Vito Di Noto[a,b,*], Enrico Negro[a,b]

[a] Dipartimento di Scienze Chimiche, Università di Padova, Via Marzolo 1, I-35131 Padova, PD, Italy
[b] Istituto di Scienze e Tecnologie Molecolari, ISTM-CNR, Dipartimento di Scienze Chimiche, Via Marzolo 1, I-35131 Padova, PD, Italy

ARTICLE INFO

Article history:
Received 12 June 2009
Received in revised form 4 August 2009
Accepted 6 August 2009
Available online 14 August 2009

Keywords:
PEM fuel cell
Oxygen reduction reaction
Pt–Rh carbon nitride electrocatalysts
CV-TF-RDE method
X-ray diffraction

ABSTRACT

In this paper the preparation of a new bimetal electrocatalyst for the oxygen reduction reaction (ORR), which is one of the most important bottlenecks in the operation of polymer electrolyte membrane fuel cells (PEMFCs), is described. This material was synthesized through a pyrolysis process of a zeolitic inorganic–organic polymer electrolyte (Z-IOPE-like) precursor, followed by suitable washing and activation procedures of the product. The electrocatalyst, whose active sites consist of platinum and rhodium, was: (a) extensively characterized from the chemical, structural, morphological and electrochemical points of view and (b) used to prepare a membrane-electrode assembly (MEA) which was tested under operative conditions in a single-cell configuration. It was observed that, with respect to a reference material based on supported platinum, rhodium did not compromise the performance of the electrocatalyst in the ORR. This behaviour was interpreted in the framework of a general model concerning the enhancement of ORR performance in bimetal systems supported on carbon nitrides. Finally, the material shows a slightly better tolerance toward a few common contaminants for the ORR such as methanol and chloride anions, typical of direct methanol fuel cells (DMFCs) and vehicular applications, respectively.

1. Introduction

In recent years, both the academic and the industrial worlds have spent significant efforts for the development of viable fuel cells [1–3]. These electrochemical devices convert the chemical energy of their reagents into direct electric current and heat [4]. An interesting family of fuel cells is the one based on polymer proton-conducting membranes (Polymer Electrolyte Membrane Fuel Cells, PEMFCs) [5]. These devices use mostly hydrogen or methanol–water solutions as fuel, which are fed directly into the system (Direct Methanol Fuel Cells, DMFCs) [6]. PEMFCs operate at low temperatures (under 130 °C), and can reach a very high efficiency (up to ≈65%), much higher than that characterizing traditional thermal engines (at most ≈40% due to Carnot limits) [7]. These features make PEMFCs very attractive for several applications, such as in the automotive field [2,8] and to provide power to consumer's portable electronic devices such as laptop computers and MP3 players [9]. However, PEMFCs are not in widespread use yet as there are still several drawbacks to be overcome including durability, high cost of materials and performance, which still need to be optimized [10–12]. In particular, one research area which has recently drawn much attention is the one dealing with the improvement of the electrocatalysts mounted at the cathode of the cell, where the oxygen reduction reaction (ORR) takes place [10]. ORR is very sluggish, leading to very high overpotentials which seriously degrade the operating potential of the cell [10,13]. Furthermore, state-of-the-art electrocatalysts are very expensive as they consist of nanoparticles of crystalline platinum supported on active carbons featuring a very large surface area [14]. The most widespread procedure to prepare these electrocatalysts consists in the impregnation of the supporting active carbons with appropriate platinum salts followed by their reduction through chemical methods [15]. Recently, our research group was involved in the development of new synthesis routes to obtain new electrocatalysts [16–18]. In summary, very interesting results were obtained from a reaction pathway where a homogeneous, nitrogen-containing hybrid inorganic–organic precursor is prepared and subsequently pyrolised, washed and activated to yield the final materials [19–24]. These systems consist of active sites with the desired metal composition supported on a carbon nitride matrix. The nitrogen atoms of latter were meant to coordinate the metal species of the active sites, stabilizing the interface with the support.

* Corresponding author at: Dipartimento di Scienze Chimiche, Università di Padova, Via Marzolo 1, I-35131 Padova, PD, Italy. Tel.: +39 049 827 5229; fax: +39 049 827 5229.
E-mail address: vito.dinoto@unipd.it (V. Di Noto).

0378-7753/$ – see front matter © 2009 Elsevier B.V. All rights reserved.
doi:10.1016/j.jpowsour.2009.08.005

It is well-known that one possible approach to obtain improved electrocatalysts for the ORR is to use platinum together with a first-row transition metal such as Cr, Fe, Co, Ni and others [10,15,25–28]. With respect to Pt-based reference systems, this procedure leads to materials with a slightly lower overpotential. This approach has already been attempted, leading to very promising results obtained with carbon nitride systems featuring platinum–nickel and platinum–iron active sites [16–19,21,22,29]. The aim of this paper was the preparation of a new electrocatalyst material consisting of a carbon nitride matrix supporting active sites made of platinum and rhodium. This study was carried out in order to explore the potential of this new preparation procedure to obtain active bimetal carbon nitride systems based on Pt and Rh for use at the cathode of PEMFCs and DMFCs, and to explore the effect of a second-row transition element on the performance of platinum-based ORR electrocatalysts. For the first time, it was found that it is possible to synthesize a Z-IOPE using as reagents a rhodium chloride complex and a platinum cyanometalate, further confirming the flexibility of this type of preparation protocol. The obtained Z-IOPE, after a pyrolysis process showed that: (a) nitrogen was incorporated in the support matrix; (b) a good control of the metal stoichiometry was achieved and (c) platinum–rhodium alloys were not detected. This latter behaviour is quite unusual and different if compared with other typical bimetal electrocatalysts described elsewhere [15,30,31]. A good performance in the ORR both in "ex situ" measurements and at the cathode of a membrane-electrode assembly (MEA) was determined for the proposed bimetal electrocatalyst, thus demonstrating that the presence of rhodium did not compromise significantly the performance of the material.

2. Experimental

2.1. Reagents

Rhodium trichloride, hydrate (Rh assay: 38%), and potassium tetracyanoplatinate, hydrate (Pt assay: 45.34%) were obtained from ABCR GmbH. D(+)-sucrose, biochemical grade, was Acros reagent. EC-20 was received from ElectroChem, Inc. (nominal Pt loading: 20%) and used as a reference electrocatalyst consisting of supported Pt. Vulcan XC-72R carbon black was provided as a courtesy by Carbocrom s.r.l. and washed with H_2O_2 10 vol.% prior to use. All the other reagents were used as received.

2.2. Preparation of the materials

4 mmol of $RhCl_3 \cdot xH_2O$ (1.080 g) and 4 mmol of $K_2Pt(CN)_4$ (1.721 g) were each dissolved into the minimum amount of ultrapure water (Milli-Q, Millipore), yielding a deep red (A) and a transparent solution (B), respectively. 8.92 g of sucrose were dissolved into the minimum amount of ultrapure water; the resulting solution was divided into two identical aliquots (C). One aliquot of sucrose solution (C) was added to each of the metal-containing solutions, yielding a deep red (A + C) and a transparent (B + C) solution, respectively. (A + C) and (B + C) were then mixed together. The thus obtained solution (A + B + C) was stirred for 15 min and allowed to rest overnight. A clear deep red solution was obtained, which was then transferred into a quartz tube and brought to 65 °C in a rotovapor to eliminate the excess solvent. A sol → gel transition immediately occurred giving so rise to a homogeneous, transparent light orange gel (D) which contracted and expelled water in the course of a few days due to a gel → plastic process. The resulting plastic material (E) was then dried at 120 °C for 16 h and decomposed at 300 °C for 2 h yielding a deep brown, coarse material (F). The whole thermal procedure was performed under a dynamic vacuum of 10^{-3} bar. (F) was ball-milled for 3 h and thermally treated at 600 °C under a dynamic vacuum of 10^{-3} bar for 2 h. The resulting product consisted in a black powder (G) which was ball-milled for 2 h, washed three times with ultrapure water, treated with H_2O_2, 10 vol.% and eventually dried under an IR lamp, giving so rise to the final electrocatalyst material labelled Pt–Rh–CN 600.

2.3. Instruments and methods

The metal composition of the material was determined by ICP-AES using the method of standard additions. Emission lines were: λ(Pt) = 214.423 nm, λ(Rh) = 343.489 nm, λ(K) = 766.490 nm. Further details on the experimental set-up, mineralization procedure and elemental analyses are reported elsewhere [19]. Thermal analyses were carried out on a High-Res modulated TGA 2950 thermogravimetric analyzer produced by TA Instruments, in an open platinum pan and in a temperature range from 30 to 1000 °C. TGA profiles of samples were measured both in an inert N_2 and in an oxidising air atmosphere. FT-IR measurements in both medium- and far-FT-IR were collected on a Nicolet FT-IR Nexus spectrometer, at a resolution of 4 cm^{-1}. MIR measurements were derived by averaging 1000 scans. Samples were dispersed in anhydrous KBr pellets and sealed in a cell with KBr windows filled with N_2 inert atmosphere. Far-IR spectra were derived by averaging 1000 scans. Measurements were carried out on samples spread as thin films on a polyethylene window with nujol. Baseline correction was performed with Nicolet FT-IR Nexus spectrometer software. Micro-Raman spectra were collected on a home-made instrument, composed of: (a) a double Czerny-Turner monochromator, at a focal distance of 400 mm and a grating of 1800 lines mm^{-1} blazed at 5000 Å; (b) a Spectra-Physics Stabilite 2017 Argon Ion Laser, excitation line set at 514.15 nm, acting as the light source; (c) an Olympus BX-41 confocal microscope equipped with a 50x objective (d) a Jobin-Yvon Symphony CCD detector system, cooled with liquid nitrogen. XRD data were collected on a Bruker D8 Advance Diffractometer equipped with a Göbel mirror and a Cu-K_α source (40 kV, 40 mA) in the 2θ range 2–80°, with 0.02° step and an integration time of 15 s. Standard images collected with backscattered electrons were recorded using a Cambridge Stereoscan 250 Mark 1 electron microscope at an acceleration voltage of 20 kV. XPS analyses were run on a PerkinElmer Φ5600ci spectrometer with standard Al-K_α radiation (1486.6 eV) operating at 350 W. Working pressure was lower than 5×10^{-8} Pa. The spectrometer was calibrated by assuming binding energy (BE) of the $Au4f_{7/2}$ line at 83.9 eV with respect to the Fermi level. The standard deviation for BE values was 0.15 eV. Survey scans (187.85 eV pass energy, 1 eV $step^{-1}$, 50 ms $step^{-1}$) were obtained in the 0–1300 eV range. Detailed scans (58.7 eV pass energy, 0.2 eV $step^{-1}$, 50 ms $step^{-1}$) were recorded for the O1s, C1s, N1s, Cl2p, K2p, Rh3d and Pt4f regions. Atomic composition was evaluated after Shirley-type background subtraction [32], with sensitivity factors supplied by PerkinElmer [33]. Samples were introduced directly into the XPS analytical chamber by a fast entry lock system. Peaks were assigned on the basis of the values reported in the NIST XPS Database [33–35].

2.4. Electrode preparation and electrochemical measurements

Porous electrodes were prepared according to a procedure described elsewhere [22]. 12 mg of Pt–Rh–CN 600 material was added to the same amount of XC-72 R carbon black. The resulting mixture was ball-milled for 3 h to obtain a homogeneous dispersion. 17.16 mg of the resulting powder was placed in a glass vial, together with 3.33 g of ultrapure Milli-Q water (Millipore) and 31 μL of a commercial Nafion solution (Aldrich, 5 wt%). The resulting ink was sonicated for about 1 h to ensure a good homo-

Table 1
Chemical composition of the Pt–Rh–CN 600 material and of EC-20 reference.

Material	wt%					Formula
	Pt[a]	Rh[a]	K[a]	C[b]	N[b]	
Pt–Rh–CN 600	15.21	6.84	0.85	60.17	1.72	$K_{0.28}[PtRh_{0.85}C_{64}N_{1.6}]$
EC-20[c]	20	–	–	80	–	$[PtC_{65}]$

[a] Determined by ICP-AES spectroscopy.
[b] Determined by elemental analysis.
[c] Commercial material produced by Electrochem Inc. Nominal values.

geneity. 15 μL of the ink were then transferred to the top of a freshly polished glassy-carbon electrode tip with an active diameter of 5 mm, yielding an overall Pt loading of about 30 μg Pt cm^{-2}. Water was then removed from the ink by evaporation under an IR lamp. The same procedure was applied to prepare the electrode to test the EC-20 reference material, with the difference that no XC-72 R was added, resulting in an overall Pt loading of about 30 μg Pt cm^{-2}. The overall thickness of the electrode layer was ca. 1.4 and 0.7 μm for Pt–Rh–CN 600 and EC-20 electrocatalyst, respectively. The tip was then mounted on an EDI 101 rotating electrode attached to a CTV 101 speed control unit, both produced by Radiometer Analytical. The resulting system was used as a working electrode in order to test the ORR activity of the electrocatalyst materials. A platinum counter-electrode was adopted. An $Hg/HgSO_4/K_2SO_4$ (saturated) reference electrode was placed in a separate compartment and connected to the main electrochemical cell by a salt bridge filled with a $KClO_4$ saturated solution. The cell was filled with a 0.1 M $HClO_4$ solution, and electrochemical measurements were performed at 60 °C by rotating the electrode at a single angular speed of 1600 rpm [10]. Data were collected on a Potentiostat/Galvanostat model 263A, EG&G Instruments. Materials were activated by cycling the working electrode between 0.05 V and 1.15 V vs. NHE until the voltammograms became stable. High-purity nitrogen, oxygen and carbon monoxide (Air Liquide) were used to saturate the electrochemical cell and to test the electrocatalytic performance of the materials in various atmospheres. The electrochemical performance of the materials in the ORR was evaluated by collecting linear sweep voltammetries (LSVs) from 0.05 to 1.15 V at 5 mV s^{-1}. The poisoning effect of methanol and chloride anions in the ORR was evaluated as described elsewhere by collecting LSVs at 5 mV s^{-1} at increasing methanol and chloride anion concentrations of 0, 0.1, 0.5, 1 M and 10^{-4}, 10^{-3}, 10^{-2} M, respectively [36]. The geometric current density (expressed as mA cm^{-2}) was obtained by subtracting the trace of the material collected in a pure nitrogen atmosphere from those of the same system measured in a pure oxygen atmosphere, and then by normalizing the resulting currents on the geometric area of the disk electrode (~0.196 cm^2). CO adlayer stripping measurements were performed as described elsewhere [37]. First, pure CO was used to saturate at 1 atm the electrochemical cell; second, the electrode was set at 0.2 V vs. NHE for 10 min in order to coordinate CO ligands to active sites. Finally, the electrochemical cell was saturated with pure nitrogen at open-circuit potential (OCP) and then a stripping process was performed from 0.05 to 1.15 V vs. NHE at 20 mV s^{-1} in order to oxidise the adsorbed CO.

2.5. MEA preparation and tests in a single fuel cell

A MEA was assembled according to a procedure described elsewhere [29] mounting the EC-20 reference at the anode and the Pt–Rh–CN 600 at the cathode using as a proton-conducting electrolyte a commercial Nafion 117 (N117) membrane. The configuration of the resulting membrane-electrode assembly (MEA) is: EC-20/N117/Pt–Rh–CN 600. The platinum loading on both electrodes was set equal to about 0.4 mg cm^{-2}. A commercial MEA (ElectroChem Inc.) having an active area of 1 cm^2 and mounting at both the anode and the cathode the EC-20 electrocatalyst with a loading of 1 mg Pt cm^{-2}, was used as reference and tested in exactly the same conditions. The electrochemical activity of the cathodic electrocatalysts was evaluated using pure hydrogen as a fuel and pure oxygen as oxidant. The temperatures of the cell and gases were 80 and 87 °C, respectively. The hydrogen and oxygen flow rates were 800 and 2000 ml min^{-1}, respectively. The back pressure of the fully humidified gases was kept at 4 bar. The single-cell tests were carried out in a 5 cm^2 single-cell with one channel serpentine flow fields for both the anodic and the cathodic side. The performance of the MEAs was determined as follows. Polarization curves were collected continuously from open-circuit potential (OCP) up to 0.1 V at 5 mA s^{-1} until the system reached stability. The final polarization curve was collected immediately afterwards. The performance of the MEAs in the kinetically controlled regime was evaluated by collecting a polarization curve at 0.1 mA s^{-1} from OCP up to ca. 0.88 V. The polarization curves were not corrected for internal resistance losses.

3. Results and discussion

3.1. Chemical composition of Pt–Rh–CN 600 electrocatalyst

Elemental analysis and inductively coupled plasma atomic emission spectroscopy (ICP-AES) measurements allowed to determine the chemical composition of the Pt–Rh–CN 600 material. Results are reported in Table 1. The data of Table 1 indicate that the Pt/Rh molar ratio of the product (i.e., 1.18) is quite similar to that of reagents (i.e., 1). In addition, a small fraction of potassium is present in the chemical composition of the product. The nitrogen content of the material is lower than 2% and no hydrogen was detected. In accordance with other studies [16,19,20,22], these results confirm that the synthesis protocol adopted here allows to obtain products characterized by: (a) a good modulation of the relative amounts of the desired metals (in this

Table 2
Data derived from TGA curves in oxidising atmosphere.

Material	Water adsorption (%)[a]	T_{MO} (°C)[b]	Δwt% T_{MO}[c]	Residue (%)[d]
Pt–Rh–CN 600	4.77	346	65.8	28.72
EC-20	1.36	403	63.2	20.73

[a] Value determined at $T = 100$ °C.
[b] Temperature of material oxidation (T_{MO}).
[c] Mass elimination at T_{MO}.
[d] Value determined at $T = 500$ °C.

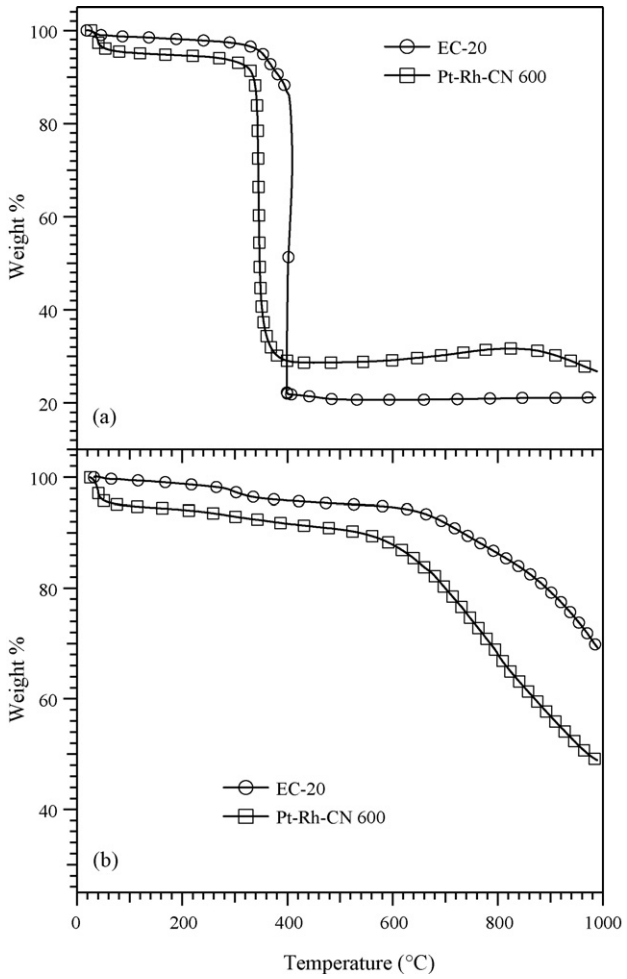

Fig. 1. Thermogravimetric profiles of Pt–Rh–CN 600 (□) and EC-20 (○). Measurements performed in N_2 (a) and air (b) atmospheres.

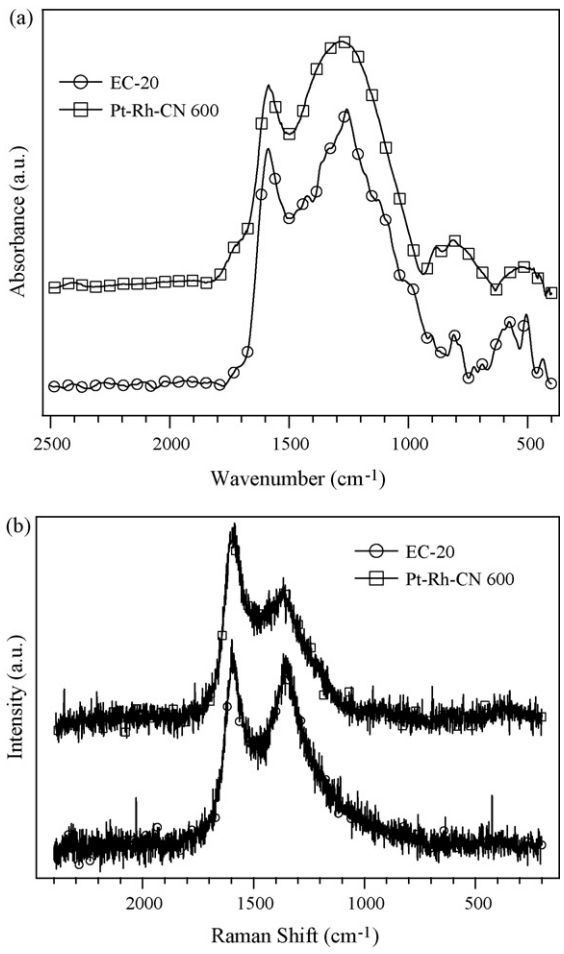

Fig. 2. Vibrational spectra of Pt–Rh–CN 600 (□) and EC-20 (○). (a) MIR and (b) micro-Raman profiles.

case Pt and Rh); (b) a small amount of potassium, which witnesses the presence of anionic complex species supported on the carbon nitride layered structure of Pt–Rh–CN 600; (c) a small fraction of nitrogen and (d) no hydrogen, thus suggesting that the graphitization of the matrix is complete, giving so rise to the formation of electrocatalysts with a good electrical conductivity.

3.2. Thermogravimetric studies

Fig. 1 shows the thermogravimetric profiles of investigated materials, and Table 2 reports the thermal parameters determined from TG curves. A careful analysis of results indicates that, with respect to the EC-20 reference, the Pt–Rh–CN 600 material is more hygroscopic. Indeed, the mass loss at $T < 100\,^{\circ}C$ of Pt–Rh–CN 600 material is more than three times higher with respect to that of EC-20 both in an inert and in an oxidising atmosphere. Measurements performed under air atmosphere revealed that Pt–Rh–CN 600 and EC-20 are thermally stable up to 360 °C and 380 °C, respectively. The residuals in air atmosphere at $T > 500\,^{\circ}C$ are consistent with the metal assay of the materials determined through ICP-AES. It should be observed that the mass residue of Pt–Rh–CN 600 is slightly higher with respect to that expected on the basis of the metal assays owing to the formation of oxides and carbon nitrides at high temperatures.

3.3. Structural characterization

3.3.1. Vibrational spectroscopy studies

Structural information on the Pt–Rh–CN 600 material was obtained by micro-Raman and vibrational studies performed in the far-FT-IR (FIR) and mid-FT-IR (MIR). MIR and micro-Raman spectra are shown in Fig. 2a and b, respectively. Fig. 3 reports the FIR spectra of materials. The correlative assignments of vibrational peaks, summarized in Table 3 [22,38–40], allow to reveal two main spectral characteristics of Pt–Rh–CN 600 material, i.e.: (a) modes

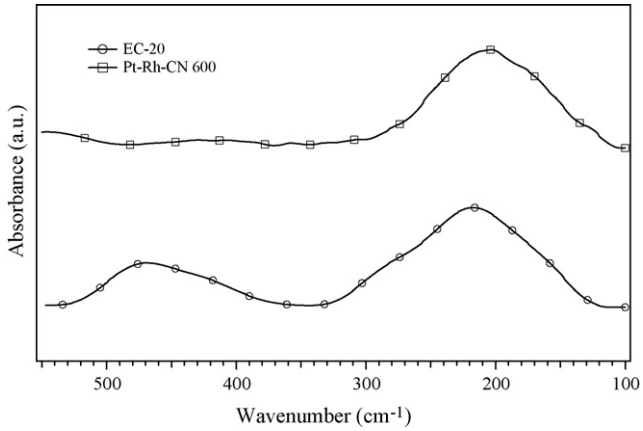

Fig. 3. FIR spectra of Pt–Rh–CN 600 (□) and EC-20 (○).

Table 3
MIR, FIR, Fourier transform IR (FT-IR) and micro-Raman band assignments of Pt–Rh–CN 600 and EC-20 electrocatalyst materials.

Pt–Rh–CN 600[a]		EC-20[a]		Band assignment[b,c]	Reference
IR	Raman	IR	Raman		
3505 (sh, w)		3500 (sh, vw)		ν^{free}(OH)	[22]
3430 (w)		3432 (s, broad)		ν(OH)	[22]
3308 (w, broad)		3251 (sh, vw)		ν^{hy}(OH)	[22]
3030 (sh, vw)				Aromatic ν(CH)	[38]
1711 (sh, w)		1710 (sh, w)		ν(COO)	[22]
1584 (s)	1593 (vs)	1588 (vs)	1595 (vs)	G-band in-plane stretching: (a) IR E_{2u} and (b) Raman E_{2g}	[22]
		1430 (w)		A_{2u}	[22]
1349 (sh, vw)	1362 (m)	1327 (w)	1349 (s)	D band, A_{1g} longitudinal acoustic wave	[22]
1277 (vs)		1258 (vs)		ν(C–O), ether	[22]
1130 (sh, vw)		1115 (vw)		ν(C–O), phenolic	[22]
1048 (sh, vw)		1020 (sh, vw)		ν(C–O), alcoholic	[22]
990 (sh, vw)				ν(C–C) of olefinic bonding of sp^2 structure	[22]
884 (w)				Heterocyclic ring "breating"	[38]
820 (w)		800 (w)		A_{2u} (oop)	[22]
760 (sh, w)				Graphite-like sp^2 domains	[39]
546 (vw)				ν(Pt–O)	[40]
		470 (w)		ν(Pt–C)	[40]
430 (vw)		420 (w)		oop bending mode	[22]
206 (w)		215 (vw)		Graphitic A_g lattice vibrations	[22]

[a] Relative intensities are reported in parentheses: vs, very strong; s, strong; m, medium; w, weak; vw, very weak; sh, shoulder.
[b] ν, stretching; oop, out-of-plane.
[c] Assignments performed correlatively on the basis of [22,38–40].

associated with the carbon nitride backbone matrix and (b) modes associated with functional groups such as ethers, phenols, alcohols and carboxyls present on the surface of the carbon nitride grains. Of particular interest are the spectral features associated with graphite-like materials which are detected in the region between 1800 and 1000 cm^{-1}. The two peaks, detected in the micro-Raman spectra at about 1590 and 1360 cm^{-1} were assigned respectively to the graphitic Raman-active E_{2g} mode (G) and to the A_{1g} lattice vibration (D) [22]. It is expected that in typical amorphous carbon materials G and D bands are infrared inactive, while in the MIR spectra of the Pt–Rh–CN 600 material they are detected. This evidence was attributed to the substitution of carbon atoms with nitrogen and to the breakdown of the k-selection rule originated from the considerable structural disorder in the graphitic-like structure of the Pt–Rh–CN 600 matrix [41]. The shapes of D and G FT-IR and Raman profiles reported in Fig. 2a and b are very similar to those typical of carbon nitrides having a nitrogen content ranging from 2% to 9% [42,43]. The vibrational studies on the spectral features attributed to the graphitic-like microdomains of the Pt–Rh–CN 600 material permit us to conclude that: (a) carbon atoms are found in both sp^2 and sp^3 hybridizations; (b) a fraction of sp^2 carbons are substituted by nitrogen and (c) a fraction of carbon atoms found on the surface of the carbon nitride grains are involved in the formation of oxygenated functional groups such as alcohols, ethers and phenols [22]. This latter information is clearly witnessed by the MIR bands located in the range 1280–1050 cm^{-1} (Table 3) [22]. No bands were detected in the frequency range 2000–2400 cm^{-1}, thus indicating that the C≡N groups coordinating the platinum atoms in the reagent have been incorporated in the carbon nitride matrix [38]. Inspection of FIR and micro-Raman spectra in the region below 600 cm^{-1} shows that: (a) no metal-ligand vibrations in both Pt–Rh–CN 600 and EC-20 materials are revealed and (b) two very weak features at 430 and 215 cm^{-1} are observed, which correspond respectively to the out-of-plane bending modes and to the A_g lattice vibrations typical of both graphitic materials and of β-phase carbon nitrides [22]. This evidence suggests that the metal nanoparticles are probably supported on graphitic-like carbon nitride nanometric grains. The particle grain size of the support of both Pt–Rh–CN 600 and EC-20 materials was determined using Raman G and D bands according to a procedure reported elsewhere [41]. Results indicated that the particle size of the crystalline domains of Pt–Rh–CN 600 material and EC-20 reference is 1.45 and 1.20 nm, respectively. In summary, the information obtained from vibrational studies indicates that the proposed Pt–Rh–CN 600 material consists of carbon nitride nanoparticles bearing on their surface oxygenated functionalities such as alcohol, ether and phenol groups and supporting the metal active sites.

3.3.2. XRD analysis

The powder XRD spectra of both Pt–Rh–CN 600 and EC-20 were analysed to gain information on the structural features of the prepared electrocatalyst (Fig. 4). The peaks of the EC-20 spectrum were easily assigned on the basis of other studies [22,44,45]. As expected, two phases were detected in EC-20: graphite and platinum. The former phase was detected by the (1 1 1) peak found at $2\theta \approx 25^\circ$. The metallic phase was identified owing to the peaks located at $2\theta \approx 39.9^\circ$, 46.1°, 67.6° and 81.5° associated respectively to the reflections (1 1 1), (2 0 0), (2 2 0) and (3 1 1) which are intensities typical of Pt nanocrystals with a face-centred cubic structure. The XRD profile of Pt–Rh–CN 600 shows features quite similar to those already found in the EC-20 reference. In this case the weak peak measured at $2\theta \approx 23.8^\circ$ (inset of Fig. 4) was ascribed to the

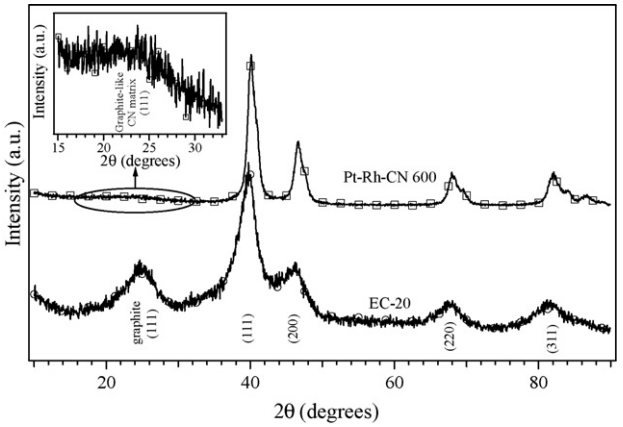

Fig. 4. Powder XRD patterns of Pt–Rh–CN 600 (□) and EC-20 (○). The Miller indexing of the patterns is shown. The inset shows the (1 1 1) peak of graphite-like CN of Pt–Rh–CN 600.

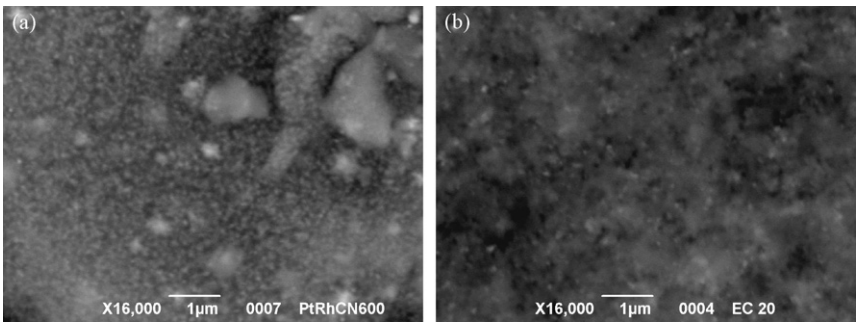

Fig. 5. SEM images of Pt–Rh–CN 600 (a) and EC-20 (b) collected with backscattered electrons.

(1 1 1) reflection of a graphitic-like carbon nitride nanoparticle. The smaller 2θ value determined on Pt–Rh–CN 600 confirms that, in accordance with vibrational studies, some sp^2 carbons of the graphitic layers are substituted by nitrogen atoms endowed with the same hybridization, which leads to a slightly larger interplanar distance. Furthermore, the remaining peaks are ascribed to two different metal phases sharing the same face-centred cubic structure. The first metal phase shows peaks located at $2\theta \approx 39.9^\circ$, 46.1°, 67.6° and 81.5°, and corresponds to platinum nanoparticles [44]. The second phase presents reflections peaking at $2\theta \approx 41.1^\circ$, 47.8°, 69.6° and 84.2°, which was assigned to rhodium metal nanoparticles [46]. It should be observed that the peak positions of these metal nanoparticles are very close to those found in pure Pt and Rh metals. Thus, a negligible alloying effect between Pt and Rh is expected. In the Pt–Rh–CN 600 the average nanocrystalline sizes of the various phases was determined with the Debye–Scherrer method using the (2 0 0) fcc reflection. Results indicated that the size of metal crystallites of Pt–Rh–CN 600 material is larger with respect to that of EC-20 reference. Indeed, for Pt–Rh–CN 600 the Pt and Rh crystallites have an average size of 6.8 and 10.9 nm, respectively, while in EC-20 reference Pt crystallites present a size of ca. 3.0 nm.

3.4. Surface studies

3.4.1. Morphology analyses

Scanning electron microscopy (SEM) was used to gain information on the surface morphology of both Pt–Rh–CN 600 and EC-20 reference. The micrographs in backscattered electrons shown in Fig. 5 show that the surface morphology of the two investigated materials is similar. Indeed, it consists of nanometric bright spots (the phase 1) immersed in a dark background matrix (the phase 2). Phase 1 was ascribed to the metal nanocrystals, and phase 2 to the graphitic-like supporting matrix.

3.4.2. XPS measurements

XPS was used to obtain information on the oxidation states and surface chemical composition of the various atoms in Pt–Rh–CN 600. Survey spectra of materials are shown in Fig. 6. The presence of carbon, oxygen and platinum was evidenced in both samples. The higher surface concentration of platinum in the EC-20 material, as evidenced in Table 4, results in a more intense Pt peak. A very strong peak has been detected in both materials at 284.4 eV, which was ascribed to the carbon atoms composing the graphitic-like structure of the support characterized by a good electrical conductivity as evidenced by the lack of charging effects [33]. In addition, the presence of nitrogen and rhodium is revealed on the surface of Pt–Rh–CN 600 material, thus pointing to their incorporation in the outer structure of the electrocatalyst. Results of quantitative analyses reported on Table 4 were obtained acquiring detailed scans of the C1s, N1s, O1s, Rh3d and Pt4f regions. In

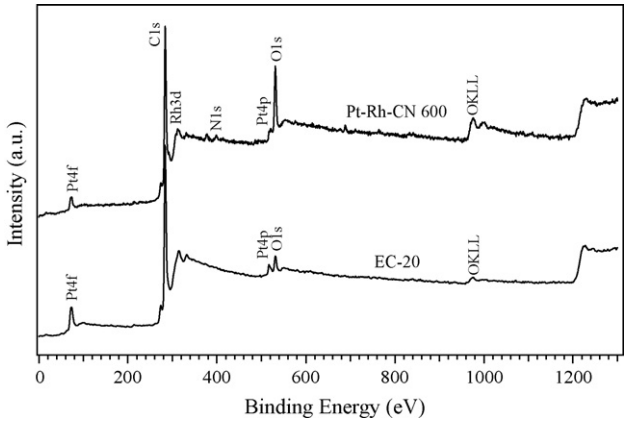

Fig. 6. XPS spectra of Pt–Rh–CN 600 and EC-20 material.

particular, it was observed that in both EC-20 and Pt–Rh–CN 600 materials, platinum shows only one component peaking at 71.3 eV. This phenomenon, which is typical of a Pt(0) specie [33], confirms that in both electrocatalysts platinum atoms found on or near the surface of the nanoparticles belong to the metal nanocrystals evidenced by powder XRD. Furthermore, in Pt–Rh–CN 600 system (Fig. 7b) two doublets of Rh nanoparticles peaking at 307.3 and 310 eV are distinguished, which are ascribed respectively to Rh(0) and Rh(III) species [33,35,47]. The Rh(III) peak is compatible with the BE value of Rh_2O_3 or Rh coordinated by a nitrogen-containing ligand. A further peak is located at 303 eV, which was attributed to an Auger Mg line deriving from contamination on the X-ray source. The approximate molar ratio between Rh(0) and Rh(III) species is 8:1 and was determined starting from the relative areas of the corresponding XPS peaks. Taken together, it is to be hypothesized that Rh nanocrystals consist of a Rh(0) core having some Rh(III) species on the surface. The Rh(III) species on the surface are detected owing to the coordination of the oxidised metal ions with ligands containing N and/or O atoms of the support or of original reagents. The oxygen peak, detected at 532 eV is essentially symmetric (Fig. 7c), and is attributed to oxygenated functional groups such as esters, aromatic rings, carboxylates, alcoholates, polyalcohol and polyether groups, thus confirming the

Table 4
Surface chemical composition (at.%) of Pt–Rh–CN 600 and EC-20 reference evaluated by XPS measurements.

Element	Pt–Rh–CN 600	EC-20
Pt	0.6	1.1
Rh	0.8	–
C	80.6	93.8
N	2.6	–
O	15.3	5.1

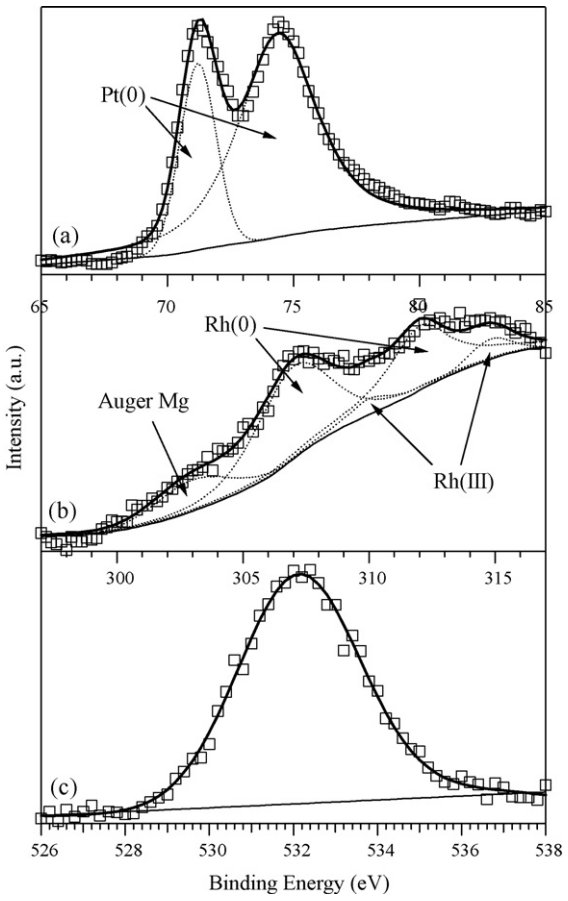

Fig. 7. Detailed XPS scans of selected regions in the spectrum of Pt–Rh–CN 600 material. (a) Decomposition of Pt 4f region; (b) decomposition of Rh 3d region and (c) O1s region.

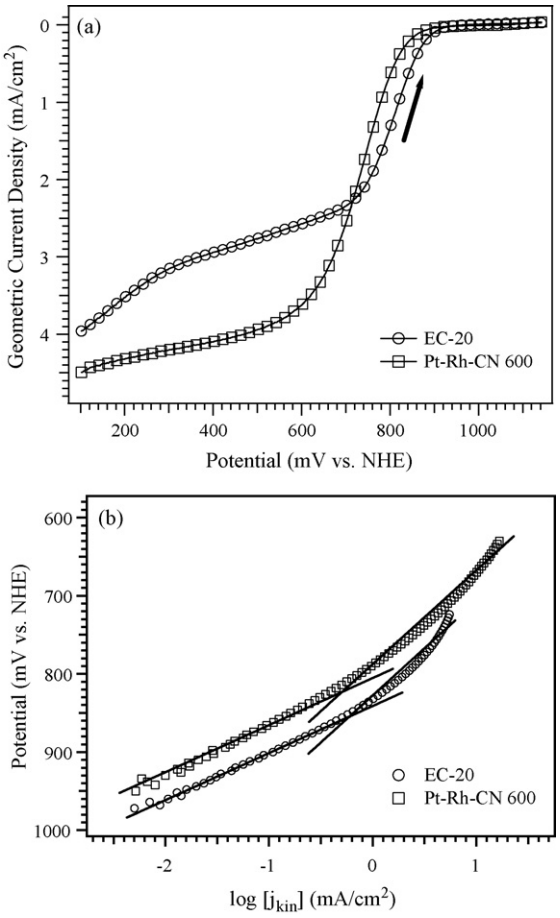

Fig. 8. (a) CV-TF-RDE profiles of Pt–Rh–CN 600 (□) and EC-20 (○); sweep rate: 5 mV s^{-1}; the electrode is rotated at 1600 rpm. (b) Tafel plots obtained from the rotating-disk data of (a) after removing the contribution due to the mass transport.

evidences previously determined by vibrational spectroscopy studies (Table 3) [22,38–40].

3.5. Electrochemical studies

Information on the performance of the materials toward the ORR was determined by cyclic voltammetry with the thin-film rotating-disk electrode (CV-TF-RDE) method as described elsewhere [10,48]. Data were obtained at only one rotation speed as the study of a Levich–Koutecky plot was outside the scope of this work. Positive-going sweeps, which were collected in exactly the same conditions, were corrected from mass transport contributions as described elsewhere [19,22]. The correction was carried out assuming that the diffusion-limited geometric current density of each material was equal to the value shown in Fig. 8a by the corresponding trace at 0.1 V vs. NHE. Positive-going sweeps were used to compare the geometric current density of the samples (Fig. 8a) and to obtain the Tafel plots reported in Fig. 8b. The most significant figures accounting of the electrochemical performance of materials are summarized in Table 5. The activation potential was evaluated in the Tafel plot at $\log(j_{kin}) = -1.5$, where j_{kin} is the mass transport corrected kinetic geometric current density, expressed as mA cm^{-2} [22]. Both the EC-20 reference and the Pt–Rh–CN 600 materials present two different Tafel slopes, equal to about 60 and 120 mV decade^{-1} in the higher and lower potential region, respectively (Fig. 8b). This coincidence indicates that the same mechanism for the ORR is found in both materials, which is corresponding to a 4-electron pathway [49]. In this case, the typical charge transfer coefficient is $\alpha = 0.5$ [50,51]. The exchange current densities were determined on the lines fitting the Tafel plots of the ORR in the high-potential region ($V > 0.85$ V vs. NHE, see Fig. 8a) at a value equal to 1220 mV (i.e., the thermodynamic potential of the ORR at 60 °C). The comparison of the kinetic performance of the Pt–Rh–CN 600 mate-

Table 5
Parameters describing the electrochemical performance of samples toward the ORR process.

Material	Geometric current density at 0.8 V (mA cm^{-2})[a]	Activation potential (mV)[b]	Tafel slope (mV decade^{-1})[c]	Exchange current density j_0 (A cm^{-2})[d]	Pt + Rh specific area (m^2 g_{Pt+Rh}^{-1})[e]
Pt–Rh–CN 600	0.63	896	60.2	$10^{-9.88}$	33.2
EC-20	1.32	935	60.2	$10^{-9.28}$	37.0

[a] Geometric current densities are determined using the CV profiles reported in Fig. 8a.
[b] The activation potential is the potential value measured in the Tafel plot at $\log(j_{kin}) = -1.5$ in Fig. 8b.
[c] Value determined in the high-potential region ($V > 0.85$ V vs. NHE).
[d] Value normalized on the geometric surface of the electrode.
[e] Determined from the CO adlayer stripping traces reported in Fig. 9.

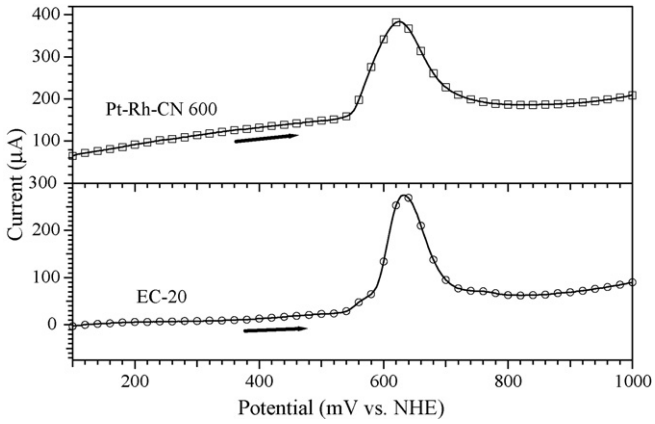

Fig. 9. CO adlayer stripping curves of Pt–Rh–CN 600 (□) and EC-20 (○). Sweep rate: 20 mV s^{-1}.

rial with the EC-20 reference points out that the latter system shows a slightly higher activation potential, i.e, 935 mV vs. 896 mV. With respect to the EC-20 reference, the intrinsic activity of Pt–Rh–CN 600 is ca. four times lower as derived from exchange current densities. CO adlayer stripping (Fig. 9) was used to determine the specific surface area of the active metal nanoparticles of the electrocatalysts [37]. The integration of the CO stripping peak of EC-20, assuming a specific charge equal to 484 μC cm_{Pt}^{-2} [52], yielded a specific surface area of 37.0 m^2 g_{Pt}^{-1}. This latter value is typical for commercial reference systems [10]. In Pt–Rh–CN 600 material it is very difficult to measure the individual Pt and Rh surface specific area owing to the fact that both these metals: (a) adsorb irreversibly CO and (b) give rise to CO stripping peaks which are overlapped at the same potential [37,52,53]. Therefore, the integration of Pt–Rh–CN 600 stripping peak of Fig. 9 will provide information on the overall specific surface area of Pt and Rh. If r_{Pt} is the average radius of the platinum nanocrystals, the average volume of a platinum nanocrystal V_{Pt} can be expressed by (1), in the simplified hypothesis of a spherical crystal:

$$V_{Pt} = \frac{4}{3}\pi r_{Pt}^3 \quad (1)$$

The weight of a single platinum nanocrystal w_{Pt} can be expressed by (2), where d_{Pt} is the density of the platinum metal:

$$w_{Pt} = V_{Pt} d_{Pt} = \frac{4}{3}\pi r_{Pt}^3 d_{Pt} \quad (2)$$

If n_{Pt} is the number of platinum moles found in the Pt–Rh–CN 600 material and W_{Pt} is the atomic weight of platinum, the number of platinum crystals N_{Pt} in the Pt–Rh–CN 600 material is:

$$N_{Pt} = \frac{n_{Pt} W_{Pt}}{w_{Pt}} = \frac{n_{Pt} W_{Pt}}{4/3\pi r_{Pt}^3 d_{Pt}} \quad (3)$$

In the hypothesis of spherical crystals, the surface area of all the platinum found in the Pt–Rh–CN 600 material can be expressed as:

$$A_{Pt} = N_{Pt} 4\pi r_{Pt}^2 = \frac{3 n_{Pt} W_{Pt}}{r_{Pt} d_{Pt}} \quad (4)$$

The same argument holds true for rhodium. The surface area of all the rhodium nanocrystals can thus be expressed by:

$$A_{Rh} = \frac{3 n_{Rh} W_{Rh}}{r_{Rh} d_{Rh}} \quad (5)$$

Now, the ratio between the overall area of platinum and rhodium nanocrystals can be expressed by:

$$\frac{A_{Pt}}{A_{Rh}} = \frac{n_{Pt} W_{Pt} r_{Rh} d_{Rh}}{n_{Rh} W_{Rh} r_{Pt} d_{Pt}} \approx 2.07 \quad (6)$$

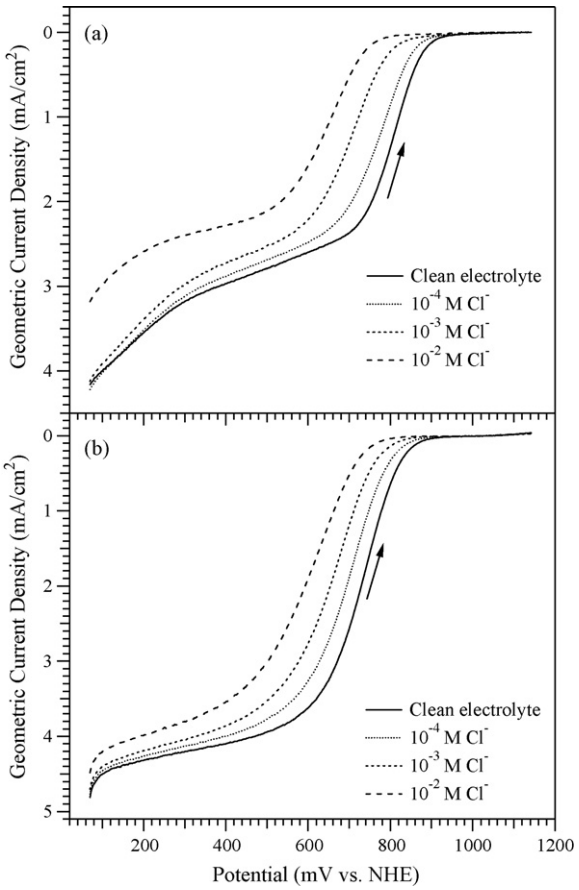

Fig. 10. Effect of Cl^- poisoning on the mass activity of the electrocatalysts toward ORR. (a) EC-20; and (b) Pt–Rh–CN 600.

This result is expected if we consider that in Pt–Rh–CN 600 the two metal phases consist of supported pure platinum and pure rhodium nanoparticles with their typical densities and atomic weights. Thus, if we consider that from material composition $n_{Pt}/n_{Rh} = 1/0.85 \approx 1.18$ and from powder X-ray diffraction results $r_{Rh}/r_{Pt} = 5.45/3.4 \approx 1.6$, Eq. (6) holds true provided that Pt and Rh nanocrystals share the same morphology, which can also be different from spherical. Indeed, literature reports that in most instances platinum and rhodium yield nanoparticles with a similar shape, either cubic (Pt) [54,55], fcc or quasi-icosahedral (Rh) [56]. Finally, the charge needed to remove one monolayer of CO from the Pt–Rh–CN 600 can be expressed by:

$$Q_{Pt+Rh} = \frac{A_{Pt} Q_{Pt} + A_{Rh} Q_{Rh}}{A_{Pt} + A_{Rh}} = \frac{2.07 A_{Rh} Q_{Pt} + A_{Rh} Q_{Rh}}{2.07 A_{Rh} + A_{Rh}} = \frac{2.07 Q_{Pt} + Q_{Rh}}{3.07} \approx 450\ \mu C/cm^2 \quad (7)$$

The specific charge of pure Rh has been assumed equal to 380 μC cm_{Rh}^{-2} [57]. Thus, it is found that: (a) the specific surface area of the metals in the Pt–Rh–CN 600 material is equal to 33.2 m^2 g_{Pt+Rh}^{-1} and (b) the specific surface of Pt is 31.9 m^2 g_{Pt}^{-1}, close to the values found in the literature for commercial systems [10]. It can be concluded that Pt–Rh–CN 600 and the EC-20 reference are characterized by an almost equivalent electrochemically active area and by similar kinetic parameters (Table 5), even if EC-20 shows a slightly larger intrinsic activity which is in line with the characteristic parameters elsewhere reported [13]. The effect of Cl^- and methanol contaminants on the ORR process is shown respectively in Figs. 10 and 11. Results demonstrate that, with respect

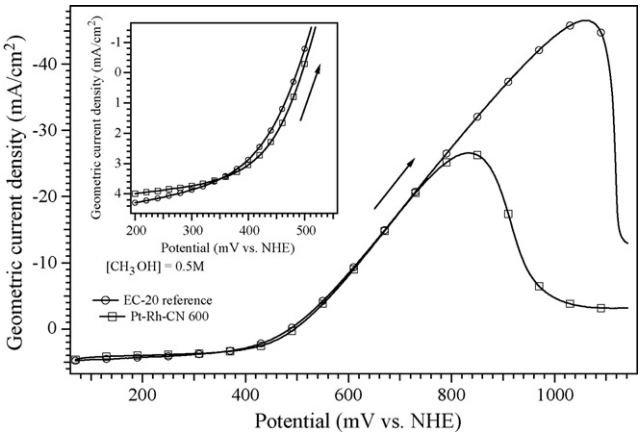

Fig. 11. Effect of methanol poisoning on the mass activity of the electrocatalyst toward the ORR. Pt–Rh–CN 600 (□) and EC-20 (○). The inset shows the traces at a geometric current density near to zero.

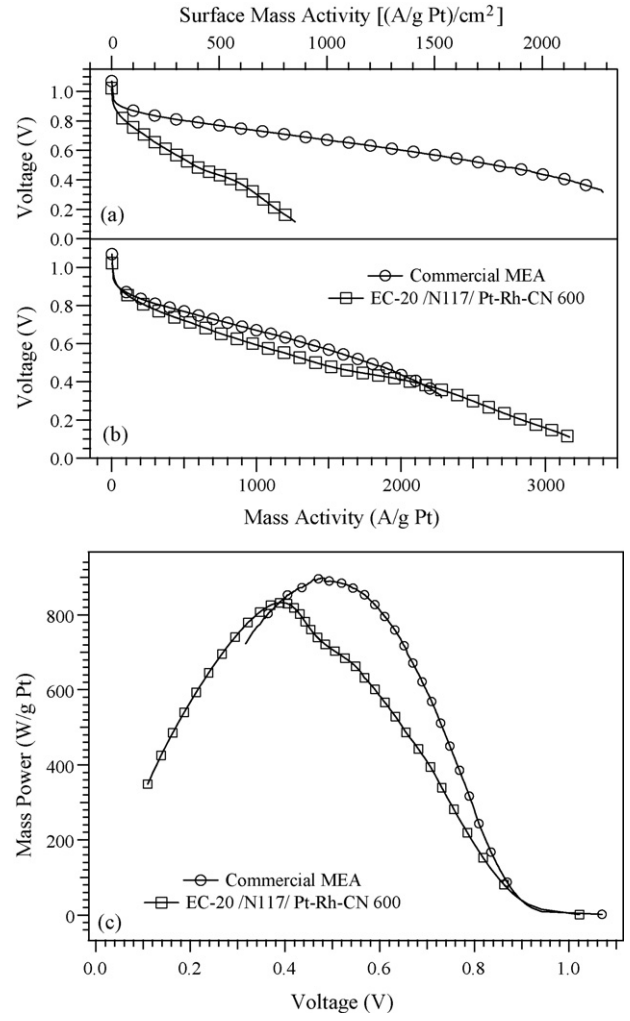

Fig. 12. Polarization curves of EC-20/N117/Pt–Rh–CN 600 MEA (□) and commercial reference MEA (○). The currents were normalized on both the active area and platinum mass (a) and on platinum mass only (b) present at the cathodic electrode. Electrical mass power profiles (c). Tests were carried out with a 5 cm^2 single-cell operating with pure H_2 at the anode and pure O_2 at the cathode. H_2/O_2 flow was 800 and 2000 ml min^{-1} at 100% RH.

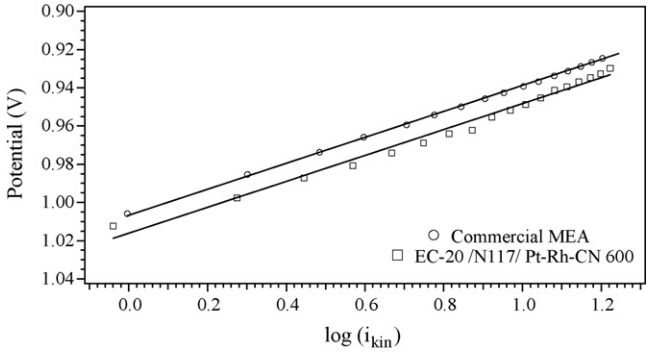

Fig. 13. Tafel plots of polarization curves collected at 0.1 mA s^{-1}. Cathode fed with pure oxygen. Current values were normalized on platinum mass at cathodic electrode. Other operating conditions as in Fig. 12.

to the EC-20 reference, the Pt–Rh–CN 600 is more tolerant toward these poisoning agents. In particular, an increase of chloride anion concentration from zero to 10^{-2} M (Fig. 10), reduces the potential of the ORR by 112 and 156 mV respectively for Pt–Rh–CN 600 and the EC-20 reference. In Fig. 11, it is observed that the maximum methanol oxidation geometric current density for the Pt–Rh–CN 600 and EC-20 is 26.6 and 46.6 mA cm^{-2}, respectively. Furthermore, in this condition the potential where the mass activity is zero is equal to 496 and 486 mV vs. NHE, respectively, for Pt–Rh–CN 600 and EC-20 (see inset of Fig. 11). On the basis of these evidences it is to be concluded that: (a) the Pt–Rh–CN 600 material has a lower capability to oxidise methanol and (b) it probably requires a slightly higher overpotential to perform the methanol oxidation reaction thus leading, with respect to the EC-20 reference, to a slightly better tolerance toward the effects of methanol crossover process.

3.6. Tests in single fuel cell

The polarization curves of the MEA prepared with the Pt–Rh–CN 600 material at the cathode, and of the commercial reference MEA are reported in Fig. 12. Two types of mass activities were considered. The first is obtained by normalizing the current to both the Pt mass and the geometric area of the cathode electrode (Fig. 12a), while the second is obtained by normalizing the current only on the Pt mass on the cathode electrode (Fig. 12b). The corresponding power curves, normalized on the mass of platinum on the cathode electrode, are shown in Fig. 12c. The figures of merit characterizing the performance of the MEAs are reported in Table 6. In particular, polarization curves were collected in the high-potential regime at 0.1 mA s^{-1} in order to study the kinetic performance of the cathodic electrocatalyst in the ORR. The Tafel plots of polarization curves thus measured are shown in Fig. 13. In this way it was possible to determine carefully the open-circuit potential and the mass activity of the electrocatalyst at 0.9 V as described elsewhere [29]. The Tafel slope of the investigated materials is similar and equal to about 60 mV $decade^{-1}$, thus suggesting that both electrocatalysts reduce the oxygen directly to water through the four-electron mechanism typical of platinum [29,49]. It should be noted that at $V < 0.85$ V, the performance of the MEA depends on a number of other factors beyond the kinetics of the electrocatalysts in the ORR, such as the transport of water and reagents, the resistance of the polymer electrolyte membrane, the electrodes and the interfaces [58]. To gauge the performance of the system in these conditions, which are very important from a practical point of view, two figures of merit were taken into account: the mass activity at 0.65 V and the mass efficiency, considered as the minimum mass of platinum mounted at the cathode necessary to produce 1 kW of electrical power [10,29,59]. This later parameter corresponds to the recipro-

Table 6
Parameters describing the electrochemical performance of MEAs in single PEMFC.

MEA	Platinum mass activity at 0.9 V (A g_{Pt}^{-1})	Platinum mass activity at 0.65 V (A g_{Pt}^{-1})	Open-circuit potential (V)[a]	Mass Efficiency (g_{Pt} kW^{-1})[b]
EC-20/N117/Pt–Rh–CN 600	34.6	765	1.013	1.20
Commercial MEA	34.0	1100	1.005	1.12

[a] The open-circuit potential is the potential value measured in the Tafel plot of Fig. 13 at $\log(i_{kin}) = 0$.
[b] The mass efficiency is the minimum cathodic platinum amount required to produce 1 kW of electrical power measured at the maximum of the curves shown in Fig. 12c.

cal of the maximum mass power measured on the power curves shown in Fig. 12c. Results summarized in Table 6 witness that the overall performance of the two investigated MEAs is quite similar, both at $V > 0.85$ V and under PEMFC "operative" regimes at $V < 0.85$ V. It is observed that the addition of Rh in the chemical composition of the proposed electrocatalyst does not lead to a significant reduction in the ORR overpotential. Finally, it should be pointed out that further work is necessary in order to determine the long-term durability of the here proposed material in a single-cell configuration.

3.7. Structural and functional models

The integration of the data deriving from the independent characterization techniques reported above prompts us to hypothesize that the Pt–Rh–CN 600 material consists of a very rough carbon nitride matrix supporting metal nanocrystals of either platinum or rhodium. It is expected that Pt and Rh nanocrystals of 6.8 and 10.9 nm diameter size are randomly distributed in the three-dimensional structure of the material. Pt–Rh–CN 600 electrocatalyst is produced from a homogeneous plastic precursor through a pyrolysis process, while the precursor is synthesized by a thermally activated polycondensation reaction. The roughness of the support matrix is provided by the elimination of the volatile components which are generated from the organic moieties of the precursor material during the pyrolysis process. The lack in the Pt–Rh–CN 600 material of a significant reduction in the overpotential of the ORR has been attributed to: (a) the poor Lewis acid character of rhodium [60] and (b) the phase segregation phenomenon taking place in this system between Rh and Pt nanoparticles. Previous studies on bimetal carbon nitride electrocatalysts for the ORR showed that an improved performance is achieved when Pt or Pd active metals in their (0) oxidation state are located next to Fe, Ni and Co complexes which act as strong Lewis acids [19–24]. In this latter case Fe, Ni and Co are found in their oxidised state. The material here proposed behaves differently. Indeed, in Pt–Rh–CN 600, platinum and rhodium are both in their (0) oxidation state and the "enhancing" effect provided by the second metal in its oxidised state is not observed owing to the fact that: (a) platinum and rhodium develop distinct phases, thus leading to a reduced probability to find two different metal atoms nearby; (b) most of Rh is found in its (0) oxidation state and (c) Rh(0) presents a poor Lewis acid character [60]. These considerations and the results here reported prompt us to conclude that the predominant ORR catalytic activity of the Pt–Rh–CN 600 material is provided by platinum active sites. The structural and functional models here proposed are also consistent with the improved tolerance of the Pt–Rh–CN 600 material towards the Cl^- and methanol contaminants in the ORR. Indeed, it is expected that a significant fraction of the active sites are bound on a hindered carbon nitride support, which prevents the site poisoning while allowing the transport of CO and O_2 molecules.

4. Conclusions

In this report a synthesis procedure for the preparation of a new Z-IOPE-like plastic precursor is described. The pyrolysis at 600 °C of this material followed by washing and activation processes resulted in a carbon nitride-based electrocatalyst for the ORR containing both platinum and rhodium. The material, labelled Pt–Rh–CN 600, was extensively characterized from the chemical, structural, morphological and electrochemical points of view. A well-modulated ratio between the metal atoms present in the Pt–Rh–CN 600 material was achieved. The structure of the electrocatalyst consisted of a very rough carbon nitride matrix supporting on the surface platinum and rhodium nanocrystals as the active sites. The electrochemical performance in the ORR of the Pt–Rh–CN 600, determined in a single-cell MEA under operative conditions, was very similar to that shown by a reference electrocatalyst supporting platinum nanoparticles on graphite, both in terms of open-circuit potential (1.013 V for Pt–Rh–CN 600 vs. 1.005 V for the reference) and mass efficiency (1.20 g_{Pt} kW^{-1} for Pt–Rh–CN 600 vs. 1.12 g_{Pt} kW^{-1} for the reference). This result indicates that Rh nanoparticles don't compromise the ORR performance owing to their: (a) phase segregation from platinum and (b) negligible Lewis acid character in the carbon nitride matrix. Finally, with respect to EC-20 reference, a slightly better tolerance in the ORR process towards typical contaminants such as chloride anions and methanol was observed for the Pt–Rh–CN 600 electrocatalyst.

Acknowledgment

This research was funded by the Italian MURST, project NUME, of FISR2003, "Sviluppo di membrane protoniche composite e di configurazioni elettrodiche innovative per celle a combustibile con elettrolita polimerico".

References

[1] K.B. Wipke, S. Sprik, J. Kurtz, J. Garbak, ECS Trans. 16 (2008) 173–184.
[2] T. Morita, K. Kojima, ECS Trans. 16 (2008) 185–198.
[3] S. Srinivasan, Fuel Cells—From Fundamentals to Applications, Springer, New York, 2003.
[4] J. Larminie, A. Dicks, Fuel Cell Systems Explained, 2nd ed., Wiley, Chichester, 2003.
[5] A. Hamnett, in: W. Vielstich, A. Lamm, H.A. Gasteiger (Eds.), Handbook of Fuel Cells: Fundamentals, Technology and Applications, vol. 1, 2003, pp. 36–43, Chichester.
[6] A. Hamnett, in: W. Vielstich, A. Lamm, H.A. Gasteiger (Eds.), Handbook of Fuel Cells: Fundamentals, Technology and Applications, vol. 1, 2003, pp. 305–322, Chichester.
[7] W. Vielstich, in: W. Vielstich, A. Lamm, H.A. Gasteiger (Eds.), Handbook of Fuel Cells: Fundamentals, Technology and Applications, vol. 1, 2003, pp. 26–30, Chichester.
[8] D.A. Masten, D. Bosco, in: W. Vielstich, A. Lamm, H.A. Gasteiger (Eds.), Handbook of Fuel Cells: Fundamentals, Technology and Applications, vol. 4, 2003, pp. 714–723, Chichester.
[9] S.R. Narayanan, T.I. Valdez, N. Rohatgi, in: W. Vielstich, A. Lamm, H.A. Gasteiger (Eds.), Handbook of Fuel Cells: Fundamentals, Technology and Applications, vol. 4, 2003, pp. 894–903, Chichester.
[10] H.A. Gasteiger, S.S. Kocha, B. Sompalli, F.T. Wagner, Appl. Catal. B: Environ. 56 (2005) 9–35.
[11] D.P. Wilkinson, J. St-Pierre, in: W. Vielstich, A. Lamm, H.A. Gasteiger (Eds.), Handbook of Fuel Cells: Fundamentals, Technology and Applications, vol. 3, 2003, pp. 611–626, Chichester.
[12] R. Borup, J. Meyers, B. Pivovar, et al., Chem. Rev. 107 (2007) 3904–3951.
[13] R. O' Hayre, S.W. Cha, W. Colella, F.B. Prinz, Fuel Cell Fundamentals, Wiley, Hoboken, 2006, p. 83.
[14] C.S. Spiegel, Designing & Building Fuel Cells, McGraw-Hill, New York, 2007, p. 202.
[15] E. Antolini, Mater. Chem. Phys. 78 (2003) 563–573.
[16] V. Di Noto, E. Negro, S. Lavina, G. Pace, PCT/IT2007/000278 Patent.
[17] V. Di Noto, E. Negro, Italian Patent PD2008A000188.

[18] V. Di Noto, E. Negro, G. Pace, S. Lavina, in: T. He (Ed.), Catalysts for Oxygen Electroreduction—Recent Developments and New Directions, Transworld Research Network, 2009, pp. 195–230.
[19] V. Di Noto, E. Negro, R. Gliubizzi, S. Gross, C. Maccato, G. Pace, J. Electrochem. Soc. 154 (2007) B745–B756.
[20] V. Di Noto, E. Negro, S. Lavina, S. Gross, G. Pace, Electrochim. Acta 53 (2007) 1604–1617.
[21] V. Di Noto, E. Negro, R. Gliubizzi, S. Lavina, G. Pace, ECS Trans. 2 (2007) 83–91.
[22] V. Di Noto, E. Negro, R. Gliubizzi, S. Lavina, G. Pace, S. Gross, C. Maccato, Adv. Funct. Mater. 17 (2007) 3626–3638.
[23] V. Di Noto, E. Negro, M. Piga, L. Piga, S. Lavina, G. Pace, ECS Trans. 11 (2007) 249–260.
[24] V. Di Noto, E. Negro, S. Lavina, N. Boaretto, M. Piga, ECS Trans. 16 (2008) 123–137.
[25] S. Srinivasan, Fuel Cells—From Fundamentals to Applications, Springer, New York, 2003, p. 243.
[26] X. Yu, S. Ye, J. Power Sources 172 (2007) 133–144.
[27] X. Yu, S. Ye, J. Power Sources 172 (2007) 145–154.
[28] T. Lopes, E. Antolini, F. Colmati, E.R. Gonzalez, J. Power Sources 164 (2009) 111–114.
[29] E. Negro, V. Di Noto, J. Power Sources 178 (2008) 634–641.
[30] H. Yang, C. Coutanceau, J.M. Léger, N. Alonso-Vante, C. Lamy, J. Electroanal. Chem. 576 (2005) 305–313.
[31] J.R.C. Salgado, E. Antolini, E.R. Gonzalez, Appl. Catal. B: Environ. 57 (2005) 283–290.
[32] D.A. Shirley, Phys. Rev. 55 (1972) 4709–4714.
[33] J.F. Moulder, W.F. Stickle, P.E. Sobol, K.D. Bomben, in: J. Chastain (Ed.), Handbook of X-ray Photoelectron Spectroscopy, Perkin–Elmer, Eden Prairie, 1992.
[34] M.P. Seah, in: D. Briggs, M.P. Seah (Eds.), Practical Surface Analysis, vol. 1, Wiley, 1990, p. 543.
[35] X-ray Photoelectron Spectroscopy Database 20, Version 3.4, National Institute of Standards and Technology, Gaithersburg, MD. http://srdata.nist.gov/XPS.
[36] T.J. Schmidt, U.A. Paulus, H.A. Gasteiger, R.J. Behm, J. Electroanal. Chem. 508 (2001) 41–47.
[37] F.C. Nart, W. Vielstich, in: W. Vielstich, A. Lamm, H.A. Gasteiger (Eds.), Handbook of Fuel Cells: Fundamentals, Technology and Applications, vol. 2, 2003, pp. 302–315, Chichester.
[38] D. Lin-Vien, N.B. Colthup, W.G. Fateley, J.G. Grasselli, The Handbook of Infrared and Raman Characteristic Frequencies of Organic Molecules, Academic Press Inc., San Diego, 1991.
[39] X.A. Zhao, C.W. Ong, Y.C. Tsang, Y.W. Wong, P.W. Chan, C.L. Choy, Appl. Phys. Lett. 66 (1995) 2652–2654.
[40] D.M. Adams, Metal-Ligand and Related Vibrations, Edward Arnold Ltd, London, 1967.
[41] F. Tuinstra, J.L. Koenig, J. Chem. Phys. 53 (1970) 1126–1130.
[42] J.H. Kaufman, S. Metin, D.D. Saperstein, Phys. Rev. B 39 (1989) 13053–13060.
[43] E.G. Wang, Prog. Mater. Sci. 41 (1997) 241–298.
[44] PCPDFWIN Database, Version 2.1, 2000, #87-0640.
[45] PCPDFWIN Database, Version 2.1, 2000, #75-2078.
[46] PCPDFWIN Database, Version 2.1, 2000, #87-0714.
[47] A.J. Urquhart, J.M. Keel, F.J. Williams, R.M. Lambert, J. Phys. Chem. B 107 (2003) 10591–10597.
[48] T.J. Schmidt, H.A. Gasteiger, in: W. Vielstich, A. Lamm, H.A. Gasteiger (Eds.), Handbook of Fuel Cells: Fundamentals, Technology and Applications, vol. 2, 2003, pp. 316–333, Chichester.
[49] N.M. Marković, R.R. Adzić, B.D. Cahan, E.B. Yeager, J. Electroanal. Chem. 377 (1994) 249–259.
[50] S. Trasatti, in: W. Vielstich, A. Lamm, H.A. Gasteiger (Eds.), Handbook of Fuel Cells: Fundamentals, Technology and Applications, vol. 2, 2003, pp. 79–87, Chichester.
[51] M. Gattrell, B. MacDougall, in: W. Vielstich, A. Lamm, H.A. Gasteiger (Eds.), Handbook of Fuel Cells: Fundamentals, Technology and Applications, vol. 2, 2003, pp. 443–464, Chichester.
[52] A. Pozio, M. De Francesco, A. Cemmi, F. Cardellini, L. Giorgi, J. Power Sources 105 (2002) 13–19.
[53] T.H.M. Housmans, J.M. Feliu, M.T.M. Korper, J. Electroanal. Chem. 572 (2004) 79–91.
[54] M.M. Koebel, L.C. Jones, G.A. Somorjai, J. Nanopart. Res. 10 (2008) 1063–1069.
[55] M. Inaba, M. Ando, A. Hatanaka, A. Nomoto, K. Matsuzawa, A. Tasaka, T. Kinumoto, Y. Iriyama, Z. Ogumi, Electrochim. Acta 52 (2006) 1632–1638.
[56] M. Marín-Almazo, J.A. Ascencio, M. Pérez-Álvarez, C. Gutiérrez-Wing, M. José-Yacamán, Microchem. J. 81 (2005) 133–138.
[57] Y.E. Sung, S. Thomas, A. Wieckowski, J. Phys. Chem. 99 (1995) 13513–13521.
[58] R. O' Hayre, S.W. Cha, W. Colella, F.B. Prinz, Fuel Cell Fundamentals, Wiley, Hoboken, 2006, p. 16.
[59] S.S. Kocha, in: W. Vielstich, A. Lamm, H.A. Gasteiger (Eds.), Handbook of Fuel Cells: Fundamentals, Technology and Applications, vol. 3, 2003, pp. 538–565, Chichester.
[60] F.A. Cotton, G. Wilkinson, Advanced Inorganic Chemistry, 2nd ed., Wiley, New York, 1966.